Volume 15
Number 29
7 August 2023
Pages 12127-12414

Nanoscale

rsc.li/nanoscale

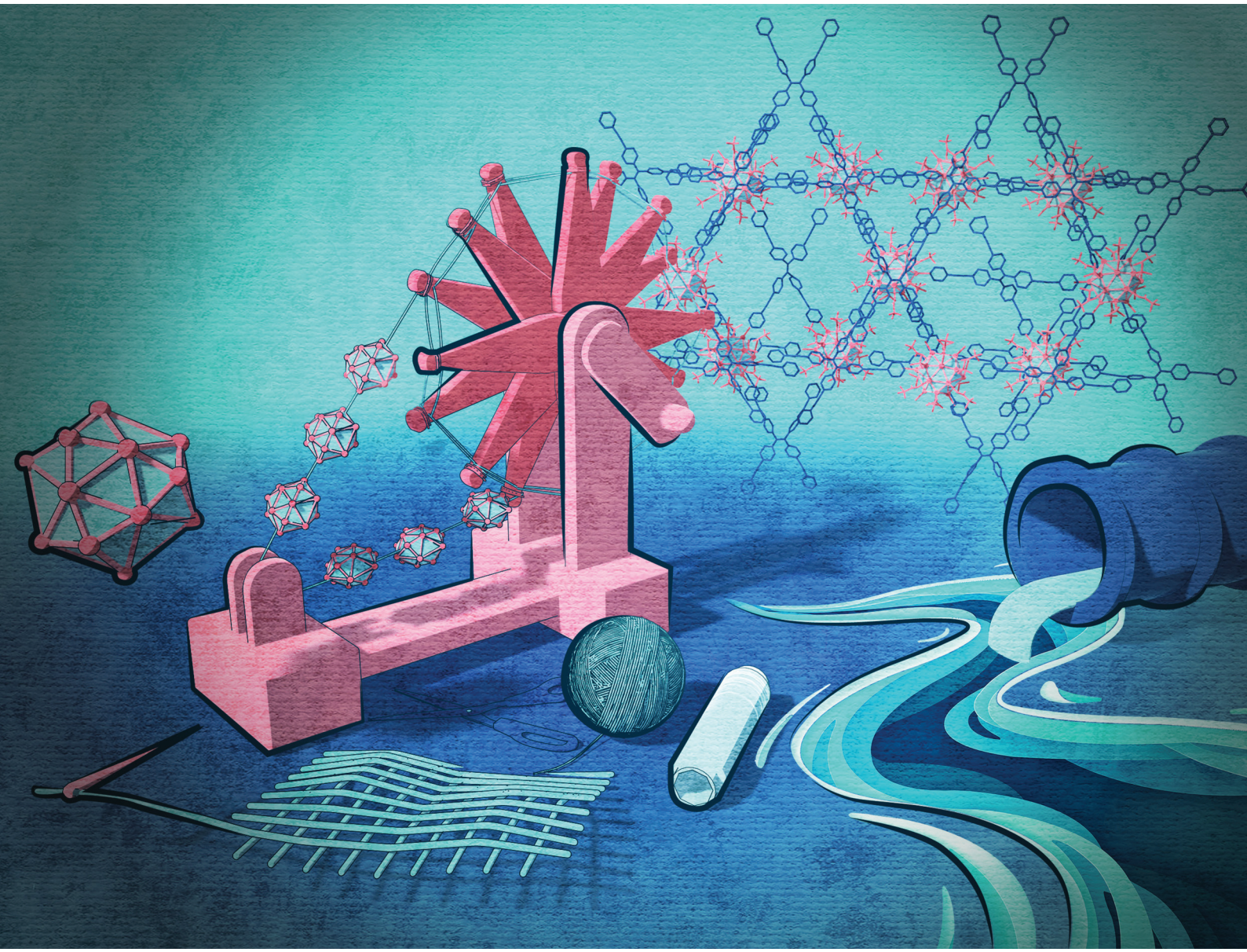

ISSN 2040-3372

ROYAL SOCIETY OF CHEMISTRY

PAPER
Saikat Das, Yuichi Negishi *et al.*
Synthesis and luminescence properties of two silver cluster-assembled materials for selective Fe^{3+} sensing

NCNST

Nanoscale

PAPER

View Article Online
View Journal | View Issue

Cite this: *Nanoscale*, 2023, **15**, 12227

Synthesis and luminescence properties of two silver cluster-assembled materials for selective Fe^{3+} sensing†

Jin Sakai,‡[a] Sourav Biswas, ‡[a] Tsukasa Irie,[a] Haruna Mabuchi,[a] Taishu Sekine,[a] Yoshiki Niihori, [b] Saikat Das *[b] and Yuichi Negishi *[a,b]

Received 25th April 2023,
Accepted 24th June 2023

DOI: 10.1039/d3nr01920a

rsc.li/nanoscale

Silver cluster-assembled materials (SCAMs) are emerging light-emitting materials with molecular-level structural designability and unique photophysical properties. Nevertheless, the widespread application scope of these materials is severely curtailed by their dissimilar structural architecture upon immersing in different solvent media. In this work, we report the designed synthesis of two unprecedented (4.6)-connected three-dimensional (3D) luminescent SCAMs, $[Ag_{12}(S^tBu)_6(CF_3COO)_6(TPEPE)_6]_n$ (denoted as **TUS 1**), TPEPE = 1,1,2,2-tetrakis(4-(pyridin-4-ylethynyl)phenyl)ethene and $[Ag_{12}(S^tBu)_6(CF_3COO)_6(TPVPE)_6]_n$ (denoted as **TUS 2**), TPVPE = 1,1,2,2-tetrakis(4-((*E*)-2-(pyridin-4-yl)vinyl)phenyl)ethene, composed of an Ag_{12} cluster core connected by quadridentate pyridine linkers. Attributed to their exceptional fluorescence properties with absolute quantum yield (QY) up to 9.7% and excellent chemical stability in a wide range of solvent polarity, a highly sensitive assay for detecting Fe^{3+} in aqueous medium is developed with promising detection limits of 0.05 and 0.86 nM L^{-1} for **TUS 1** and **TUS 2** respectively, comparable to the standard. Furthermore, the competency of these materials to detect Fe^{3+} in real water samples reveals their potential application in environmental monitoring and assessment.

Introduction

In recent years, there has been growing interest in the use of silver (Ag) nanoclusters (NCs) in various fields such as material science, chemistry, and biology.[1–4] Ag NCs are nanoscale particles of Ag, typically composed of tens to hundreds of atoms ranging between 1 and 3 nm of cluster radius.[5–12] One of the key challenges in utilizing these nanomaterials is their stability, as their properties can be highly sensitive to their environment.[5] However, recent advances in the fabrication and manipulation of Ag NCs have led to the development of cluster-assembled materials with enhanced stability and unique properties.[13–15] These materials are typically composed of a large number of Ag NC nodes that are connected through organic ligands, which serve as linkers. Organic ligands are commonly used as linkers in these materials because they can provide several advantages over other types of linkers.[14] One of the main advantages of organic ligands is their ability to form strong and selective interactions with the surface of Ag NCs. These interactions can lead to the formation of stable and well-defined extended structures, which can be tailored to exhibit specific properties and functionalities. Additionally, the use of organic ligands allows for the incorporation of diverse functional groups into the cluster-assembled materials, which can further enhance their properties and enable new applications. Organic ligands also offer a high degree of flexibility in the design and synthesis of silver cluster-assembled materials (SCAMs).[13] They can be easily modified to control the size, shape, and surface properties of the clusters, as well as the distance and orientation between them. This level of control can be crucial for optimizing the properties and performance of these materials for specific applications.[16] Generally, these materials have shown promise in sensing applications, where the small size and high surface area of the clusters can enable highly sensitive detection of a variety of analytes.[13,17]

Various SCAMs have been synthesized and their applicability in various fields studied during recent years.[18–29] The majority of these structures have a common node comprised of twelve Ag(I) atoms. The initial research in this area was conducted by Mak and colleagues, who extensively studied the use

[a]*Department of Applied Chemistry, Faculty of Science, Tokyo University of Science, Kagurazaka, Shinjuku-ku, Tokyo 162-8601, Japan. E-mail: negishi@rs.tus.ac.jp*
[b]*Carbon Value Research Center, Research Institute for Science & Technology, Tokyo University of Science, Tokyo 162-8601, Japan. E-mail: saikatdas@rs.tus.ac.jp*

†Electronic supplementary information (ESI) available. CCDC 2256626 and 2256627. For ESI and crystallographic data in CIF or other electronic format see DOI: https://doi.org/10.1039/d3nr01920a

‡These authors contributed equally to this work.

of various functional linkers to connect Ag_{12} cluster nodes in different dimensions and for different applications.[26,27,30] Subsequently, other research groups expanded this linking approach, using different synthetic protocols to connect different Ag NC nodes with various linkers.[31–37] The main focus of cluster assembly research was to ensure stability; however, the stability of the assembled materials has been greatly compromised even after the massive research output, which, in turn, negatively impacts their final application scope.[22,25,31] The dissimilar structural architecture displayed by most of these assembled materials when immersed in different solvent media is likely due to the adverse effect of solvent polarity, which can be a crucial factor affecting the stability of the frameworks.

In view of the foregoing, we herein report the designed synthesis of two new three-dimensional (3D) SCAMs, $[Ag_{12}(S^tBu)_6(CF_3COO)_6(TPEPE)_6]_n$ (denoted as **TUS 1**) and $[Ag_{12}(S^tBu)_6(CF_3COO)_6(TPVPE)_6]_n$ (denoted as **TUS 2**), that are structurally rigid by varying the linkers. Despite the difference in the linker structure, it does not affect the formation of Ag cluster node during the reaction since the other constituents remain similar. These materials exhibit excellent chemical stability in a wide range of solvent polarity. However, due to the structural change of the linkers, we observed a change in their luminescence property at room temperature, which was further utilized to assess their applicability. Both materials exhibit remarkable sensing ability for Fe^{3+} in aqueous medium, with promising detection limits comparable to the standard. Moreover, the ability of these materials to detect Fe^{3+} in real water samples demonstrates their potential application possibility.

Results and discussion

Both SCAMs were synthesized using the same facile reaction method with only the linker molecules being altered. The reaction commenced by combining $[AgS^tBu]_n$ and CF_3COOAg in a 1 : 1 (v/v) acetonitrile/ethanol solution. Simultaneously, solutions of linker molecules, 1,1,2,2-tetrakis(4-(pyridin-4-ylethynyl)phenyl)ethene = TPEPE and 1,1,2,2-tetrakis(4-((*E*)-2-(pyridin-4-yl)vinyl)phenyl)ethene = TPVPE, were prepared by dissolving them in tetrahydrofuran and dichloromethane, respectively. Then the solution of metal precursors was subsequently added to the linker solution separately and left in the dark for crystallization as depicted in Fig. 1. After a day, yellow-colored crystals formed at the interface of the two liquid layers. The single-crystal X-ray diffraction (SCXRD) analysis revealed that both the crystals are crystalized in a similar trigonal crystal system with a space group of $R\bar{3}c$ (No. 167). The scanning electron microscope (SEM) and the optical microscope images of these crystals confirm their 3D architecture (Fig. 1 and Fig. S1†). It has been evident from the images that **TUS 1** forms a rod-shaped morphology, whereas **TUS 2** forms a block-shaped morphology.

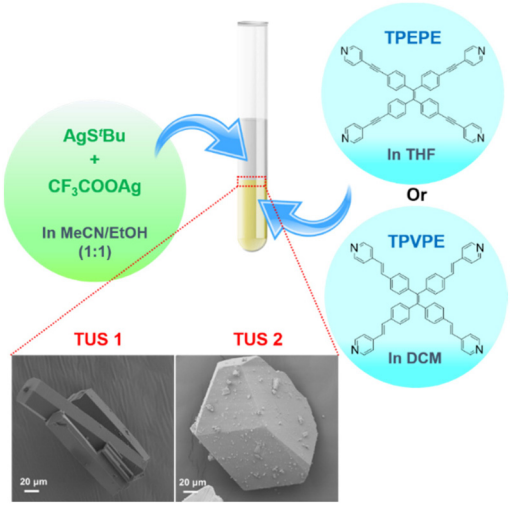

Fig. 1 Schematic representation of the reaction and crystallization process. The magnified view shows the SEM images (bottom left: **TUS 1**, bottom right: **TUS 2**) of the crystals.

It is quite interesting to note that both the crystals contain a similar Ag cluster node geometry. The twelve Ag atoms are bound together in a hollow cuboctahedron geometry through argentophilic interactions among Ag(I) atoms.[21,38] Similar to the Archimedean solids, the Ag_{12} cluster node has eight triangular facets and six convex isosceles trapezoid facets. For more depth analysis of structure anatomy, the Ag_{12} cluster node can be divided into three planes with the middle hexagonal plane consisting of six Ag atoms sandwiched by the two equilateral triangular planes (Fig. 2a). The Ag–Ag edge lengths in the middle layer range from ~3.67 Å to 3.74 Å. So, the distances between adjacent Ag atoms in the hexagonal plane are slightly higher than twice the van der Waals radius of an Ag atom and hence these connections are denoted here as virtual bonds *via* dotted lines. Although the Ag–Ag edge lengths of the two equilateral triangular planes are uniform (3 Å), the spacing distances between Ag atoms in the middle layer are uneven, resulting in Ag–Ag connections between the hexagonal plane and equilateral triangular planes that range from ~3.02 Å to 3.28 Å. Nevertheless, both distances indicate notable argentophilic interactions. Consequently, the connection between the two equatorial triangles and the middle layer forms a total of fourteen facets and creates a hollow cuboctahedron geometry (Fig. 2b).

After verifying that the Ag cluster node geometry was similar, we attempted to distinguish the dissimilarities in other connections. Nonetheless, we discovered that in both scenarios, six thiolate ligands were linked to the cluster node in the same way, with each thiolate situated outwardly on the isosceles trapezoidal facets of the cluster nodes. The bonding connections between the S and Ag atoms are likewise comparable, with each S atom bonded to two neighboring Ag atoms in the equilateral triangular plane and two neighboring Ag atoms in the hexagonal plane, with Ag–S bond distances of 2.46 Å

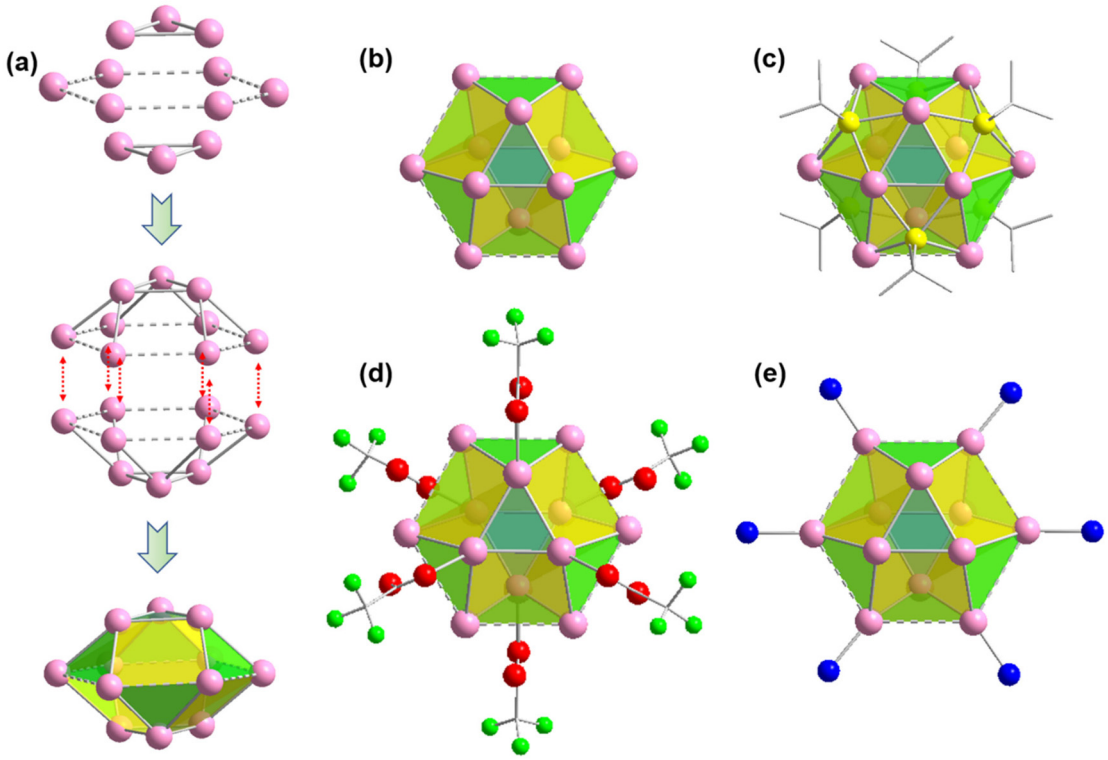

Fig. 2 (a) The formation of similar Ag_{12} cluster node architecture for both **TUS 1** and **TUS 2**. (b) Ag_{12} cluster node in a different orientation. (c) Connection of six thiolates on the Ag_{12} cluster node. (d) Connection of six CF_3COO^- on the Ag_{12} cluster node. (e) Connections of linkers on the Ag_{12} cluster node through Ag–N connectivity. Color legend: Ag, pink; S, yellow; N, blue; O, red; F, green; C, grey stick; linker part and H atoms are omitted.

and 2.52 Å, respectively. The outward attachment of six thiolate ligands on the Ag cluster node forms an octahedral geometry. Each of the cluster node in both cases is further connected to the six auxiliary CF_3COO^- ligands linked with the Ag atoms of the equilateral triangular planes through the O atom in a monodentate fashion, where the average Ag–O bond distances is ~2.42 Å. Notably, the hexagonal plane containing six Ag atoms is connected with the six linkers *via* N atom with an average Ag–N distances of 2.3 Å. So, it is quite interesting to see that although both the linker molecules have a distinct difference in structural architecture but the presence of these linkers does not affect the formation of Ag cluster nodes and their connectivity.

It has also been found that each linker is connected with four Ag cluster nodes three-dimensionally with a fixed distance. As both the linkers are connected with four cluster nodes (Fig. 3a and b) and each cluster node is linked with six linkers, so the obtained framework structure was denoted as a binodal (4.6)-connected 3D network. In both **TUS 1** and **TUS 2**, the 3D layers are stacked in ABA pattern. In case of **TUS 1**, the

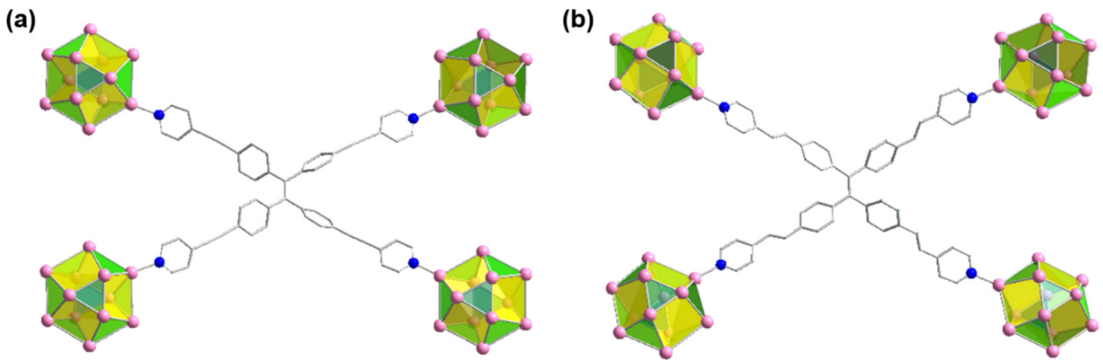

Fig. 3 Connectivity of each linker through the cluster nodes in different plane for (a) **TUS 1** and (b) **TUS 2**. Color legend: Ag, pink; N, blue C, grey stick; H atoms are omitted.

cluster nodes are separated by 27.29 Å which are linked through one linker molecule, and between the layers cluster nodes are separated with a distance of 17.89 Å whereas the interlayer distance is 5.99 Å (Fig. S2†). In case of **TUS 2**, the cluster nodes are separated by 26.84 Å which are linked through one particular linker molecule, and between the layers the cluster nodes are separated with a distance of 17.67 Å whereas the interlayer distance is 6.12 Å (Fig. S3†). As a whole, these linkers formed two new three-dimensionally linked SCAMs which are depicted in Fig. 4a and b (up to 2 layers of stacking for clear visualization).

In order to obtain additional confirmation regarding the composition of the synthesized SCAMs, we conducted X-ray photoelectron spectroscopy (XPS) analysis. The XPS survey spectra of each sample unequivocally indicate the existence of Ag, S, O, N, F, and C atoms within these crystals (Fig. S4†). These findings are further supported by the elemental dispersive spectra obtained from both **TUS 1** and **TUS 2** samples (Fig. S5†). Furthermore, the high-resolution binding energy spectra of each element in both of these SCAMs provide conclusive proof of their specific oxidation states when integrated into the structure (Fig. S6 and S7†). In both scenarios, the binding energy spectrum of Ag 3d reveals two peaks within the range of 367.4 eV to 373.5 eV. These peaks, separated by 6 eV, provide confirmation of the presence of silver solely in the +1-oxidation state. The binding energy spectrum of S 2p was examined in both cases, confirming the presence of sulfur in a −1-oxidation state. Additionally, the binding energies of O 1s validate the presence of Ag–O–C connections, while the associated binding energies of N 1s confirm the attachment of the linkers. The purity of the obtained crystals was identified by the matched powder X-ray diffraction (PXRD) patterns with the simulated ones (Fig. S8†). To assess the chemical stability, the crystals were immersed in solvent media with varying polarities. A well-matched PXRD patterns of both crystals after immersing in different solvent media suggests prospective application scope of the SCAMs (Fig. 5a and b). The thermal stability of the materials was confirmed by thermogravimetric analysis (TGA). It was observed that both SCAMs contain solvent molecules within their crystal lattice cavity, which causes an initial weight loss up to 100 °C (Fig. 5c and d). However, solubility remained a significant challenge despite the excellent stability of these materials. To counteract the issues, we dispersed both of them in water, where they showed excellent stability. UV-Vis absorption spectra of dispersed aqueous solution of both **TUS 1** and **TUS 2** exhibited a similar monotonic decrease with no notable absorption peaks as illustrated in Fig. S9a.† This observation is consistent with the solid-state absorbance spectra (Fig. S9b†). However, both SCAMs in water medium demonstrated intense emission intensities when excited at 350 nm, with **TUS 1** displaying an emission maximum at 530 nm and **TUS 2** at 561 nm (Fig. 5e). This difference in emission maximum can be attributed to the structural difference in the linkers connecting the similar Ag_{12} cluster nodes, even though both exhibited similar absorption spectra. We also identified a variation in their absolute quantum yield (QY) values, with **TUS 1** exhibiting a QY of 3.1% and **TUS 2** of 9.7%. By utilizing time-correlated single-photon counting (TCSPC), we measured the emission lifetime of both SCAMs, which was fitted with bi-exponential factors (Fig. 5f and Table S3†). The calculated average lifetime of **TUS 1** was 2.75 ns, while that of **TUS 2** was 2.33 ns. The emission spectra of the SCAMs in the solid state exhibit a red-shift, indicating the mitigation of interactions between the SCAMs and solvent molecules (Fig. S10†). Additionally, the stability of these materials was reassessed by investigating their solid-state light

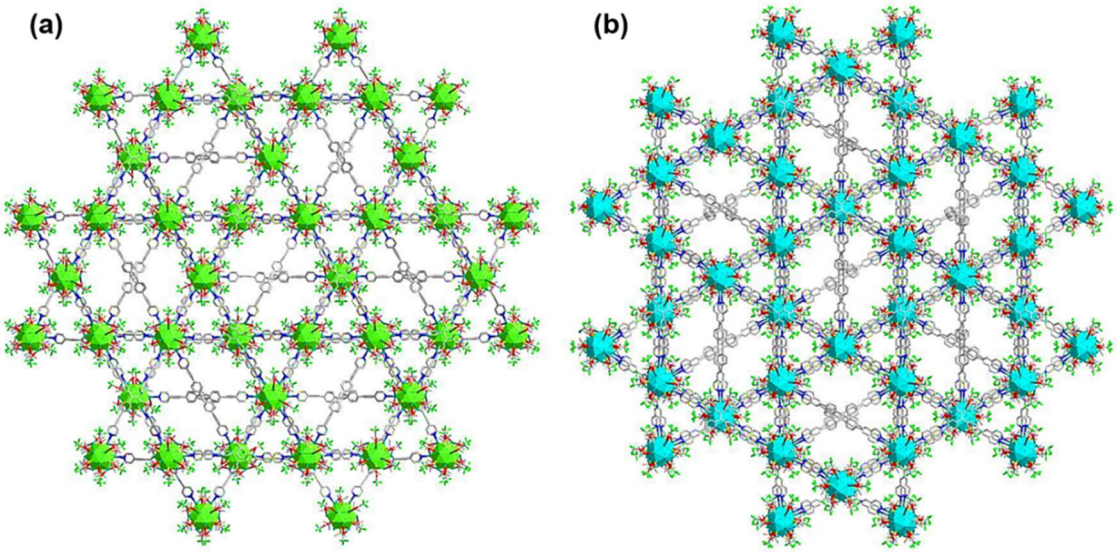

Fig. 4 3D assembly of (a) **TUS 1** and (b) **TUS 2**, irrespective of the difference in linker architecture. Color legend: Ag cluster node, bright green for **TUS 1** and cyan for **TUS 2**; S, yellow; N, blue; O, red; F, green; C, grey stick; H atoms are omitted.

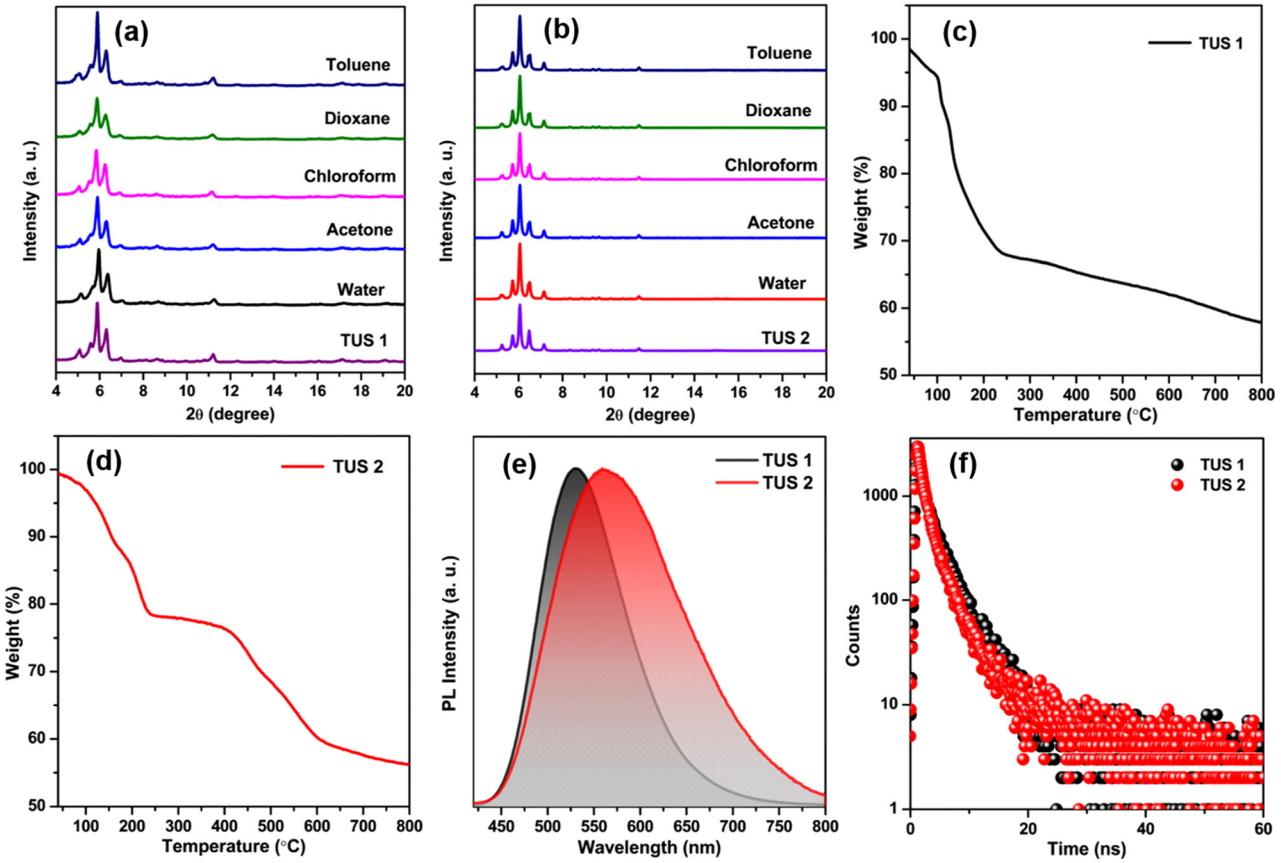

Fig. 5 Chemical stability test of (a) **TUS 1** and (b) **TUS 2** through well-matched PXRD patterns. TGA traces of (c) **TUS 1** and (d) **TUS 2**. (e) Emission of **TUS 1** and **TUS 2** while excitation at 350 nm in water medium. (f) TCSPC lifetimes of **TUS 1** and **TUS 2**.

emission properties (Fig. S11†). Notably, we observed no alteration in the emission characteristics of the SCAMs when immersed in water or toluene, suggesting their robustness and resilience to these solvents.

Due to their exceptional fluorescence characteristics and ability to withstand water, we became intrigued by the potential of these newly synthesized SCAMs for detecting metal ions in aqueous solutions. Our investigations revealed that Fe^{3+} effectively suppressed the photoluminescence (PL) emission intensities of both SCAMs at room-temperature and pH ~7.1. Furthermore, we observed a strong correlation between the degree of quenching and the Fe^{3+} concentration, suggesting the possibility of developing a highly sensitive assay for detecting Fe^{3+}. Indeed, as the concentrations of Fe^{3+} gradually increased from 0.2 nM to 10 μM, the emission intensities of **TUS 1** and **TUS 2** at the emission maxima decreased accordingly (Fig. 6a and b). However, there is a slight difference in the detection limit observed for **TUS 2** which could not detect the concentration below 1 nM concentration of Fe^{3+} (Fig. S12†). To plot the relationship between the concentrations of Fe^{3+} and the PL intensities of the two SCAMs, we used I_0/I as the *y*-axis and the concentrations of Fe^{3+} as the *x*-axis, as shown in Fig. S13 and S14.† The emission intensities of **TUS 1** and **TUS 2** are linearly related to the concentrations of Fe^{3+} in all ranges, as demonstrated by the calibration curves. To determine the limit of detection (LOD), we used the well-established 3σ method, where the LOD = $3\sigma/k$, with σ being the standard deviation of the blank samples and k being the slope of the linear calibration plot.[39] Using the calibration curves, we determined the LOD to be 0.05 nM L^{-1} for TUS 1 and 0.86 nM L^{-1} for TUS 2, which is well below the maximum permissible concentration of Fe^{3+} in drinking water (3.57 μmol L^{-1}) as required by the European Union.[39,40]

After establishing the sensing assay, we conducted careful experiments to investigate its selectivity. Since many ions often coexist in industrial effluents, it is crucial for a metal-ion sensing assay to be free from the interference of other ions. Initially, we sought to find the detection limit of most commonly seen metal ions such as K^+, Na^+, Ni^{2+}, Cu^{2+}, La^{3+}, and Cr^{3+}, but they could not be identified by either of the SCAMs (Fig. 6c and d). After that, we studied the interference of these metal ions and found no change in the detection limit of Fe^{3+} in the presence of these interfering metal ions (Fig. 6e and f). These results indicated that both SCAMs had excellent selectivity towards Fe^{3+} and were free from interference from most common metal ions. It has been observed that the UV-Vis absorption spectra of **TUS 1** and **TUS 2** undergo a slight change upon addition of Fe^{3+} solution (Fig. S15†). However, this change does not completely alter the absorption spectrum, indicating the stability of both SCAMs after the addition

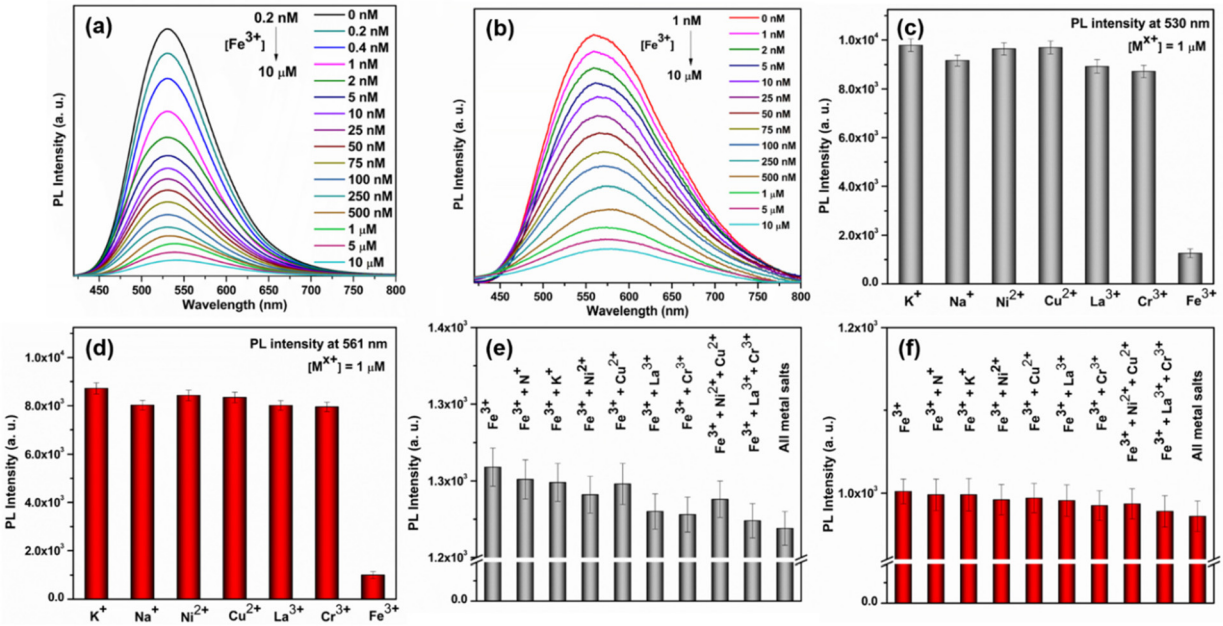

Fig. 6 (a) and (b) Fe^{3+} sensing ability of **TUS 1** and **TUS 2** respectively in aqueous medium (c) and (d) sensing ability of other metal ions by **TUS 1** and **TUS 2** respectively in aqueous medium, (e) and (f) represent the effect in the detection of Fe^{3+} while of other metal ions are present together by **TUS 1** and **TUS 2** respectively in aqueous medium.

of Fe^{3+}. The PXRD patterns of the samples also matched well after the crystals are dipped in Fe^{3+} solution, further supporting the intact structural architecture of both SCAMs (Fig. S16†). The appearance of new peaks in the absorption spectrum is mainly attributed to the adsorption of Fe^{3+} ions (Fig. S15†). This indicates the formation of some non-fluorescent complexes, which may be ascribed to the static quenching mechanism. By performing energy dispersive X-ray spectroscopy (EDS) measurements on the separated SCAMs subsequent to the sensing experiments, we have confirmed the existence of iron species attached to the surface of both SCAMs (Fig. S17†). To assess the applicability of this sensing assay using the SCAMs, we tested for the presence of Fe^{3+} in tap water and river water samples, both with and without spiking. The results from the recoveries of the spiking samples using both SCAMs demonstrate the potential of these materials for use in sensing assays (Tables S4 and S5†). Thus, the recently produced SCAMs showcase not just remarkable structural patterns but also demonstrate remarkable detection potential for Fe^{3+} in aqueous solutions. So, this research introduces a promising avenue for designing new SCAMs and utilizing them in the development of metal ion sensors that can be beneficial under more realistic circumstances and broader applications in the future.

Conclusions

In conclusion, this study reported the successful synthesis of two novel silver cluster-assembled materials by varying the linkers, resulting in a common Ag_{12} cluster node. The materials exhibit a three-dimensional layered architecture, resulting from equivalent linker connection to the node in a comparable manner. Although the materials possess remarkable stability, their solubility remains inadequate. However, these materials demonstrate remarkable luminescence properties when dispersed in aqueous medium. This property is further leveraged to efficiently detect Fe^{3+} in aqueous medium through emission quenching. These findings hold potential for the molecular-level design of new SCAMs and explore their potential application with precise correlation of structure and property.

Experimental

Synthesis of TUS 1

First, AgS^tBu (24 mg, 0.12 mmol) was dispersed under stirring in 5 mL of acetonitrile/ethanol (1 : 1, v/v) solution in a glass vial. CF_3COOAg (24 mg, 0.11 mmol) was then added to the solution and stirred until a clear solution **1** was obtained. In another glass vial, TPEPE (14.7 mg, 0.02 mmol) was dissolved in 5 mL of tetrahydrofuran to obtain a clear solution **2**. 1.5 mL of solution **2** was transferred into a Pyrex tube. After this, 1.5 mL of solution **1** was transferred into the tube. The tube was left in the dark for crystallization for 1 day, following which yellow-colored hexagonal rod-like crystals of **TUS 1** (17.4 mg) were obtained at the interface of the two liquid layers.

Synthesis of TUS 2

First, AgS^tBu (24 mg, 0.12 mmol) was dispersed under stirring in 5 mL of acetonitrile/ethanol (1 : 1, v/v) solution in a glass

vial. CF_3COOAg (24 mg, 0.11 mmol) was then added to the solution and stirred until a clear solution **1** was obtained. In another glass vial, TPVPE (14.9 mg, 0.02 mmol) was dissolved in 5 mL of dichloromethane to obtain a clear solution **2**. 1.5 mL of solution **2** was transferred into a Pyrex tube. After this, 1.5 mL of solution **1** was transferred into the tube. The tube was left in the dark for crystallization for 1 day, following which yellow-colored block-like crystals of **TUS 2** (8.6 mg) were obtained at the interface of the two liquid layers.

Author contributions

S. D. and Y. Negishi conceived the research and designed the experiments. J. S. performed the synthesis of the SCAMs. J. S., S. B., T. I., H. M. and T. S. carried out the characterization. J. S., S. B., Y. Niihori and S. D. analyzed the data. S. B., S. D. and Y. Negishi wrote the manuscript. All authors have approved the final version of the manuscript.

Conflicts of interest

There are no conflicts to declare.

Acknowledgements

This work was supported by the Japan Society for the Promotion of Science (JSPS) KAKENHI (grant no. 20H02698, 20H02552), Scientific Research on Innovative Areas "Aquatic Functional Materials" (grant no. 22H04562), Yazaki Memorial Foundation for Science and Technology, and Ogasawara Foundation for the Promotion of Science and Engineering.

References

1 I. Díez and R. H. A. Ras, *Nanoscale*, 2011, **3**, 1963–1970.
2 Y.-P. Xie, Y.-L. Shen, G.-X. Duan, J. Han, L.-P. Zhang and X. Lu, *Mater. Chem. Front.*, 2020, **4**, 2205–2222.
3 D. Li, H. Chen, X. Gao, X. Mei and L. Yang, *ACS Sens.*, 2021, **6**, 613–627.
4 Y. Tao, M. Li, J. Ren and X. Qu, *Chem. Soc. Rev.*, 2015, **44**, 8636–8663.
5 R. Jin, C. Zeng, M. Zhou and Y. Chen, *Chem. Rev.*, 2016, **116**, 10346–10413.
6 J. Yang and R. Jin, *ACS Mater. Lett.*, 2019, **1**, 482–489.
7 J. Yang and R. Jin, *J. Phys. Chem. C*, 2021, **125**, 2619–2625.
8 I. Chakraborty and T. Pradeep, *Chem. Rev.*, 2017, **117**, 8208–8271.
9 S. Biswas, A. K. Das, A. C. Reber, S. Biswas, S. Bhandary, V. B. Kamble, S. N. Khanna and S. Mandal, *Nano Lett.*, 2022, **22**, 3721–3727.
10 A. K. Das, S. Biswas, S. S. Manna, B. Pathak and S. Mandal, *Chem. Sci.*, 2022, **13**, 8355–8364.
11 S. Biswas, A. K. Das, S. S. Manna, B. Pathak and S. Mandal, *Chem. Sci.*, 2022, **13**, 11394–11404.
12 S. Biswas, S. Das and Y. Negishi, *Coord. Chem. Rev.*, 2023, **492**, 215255.
13 A. Ebina, S. Hossain, H. Horihata, S. Ozaki, S. Kato, T. Kawawaki and Y. Negishi, *Nanomaterials*, 2020, **10**, 1105.
14 S. Biswas, P. Sun, X. Xin, S. Mandal and D. Sun, in *Atomically Precise Nanochemistry*, ed. R. Jin and D. Jiang, 2023, pp. 453–478, DOI: **10.1002/9781119788676.ch15**.
15 S. A. Claridge, A. W. Castleman Jr., S. N. Khanna, C. B. Murray, A. Sen and P. S. Weiss, *ACS Nano*, 2009, **3**, 244–255.
16 X. Kang and M. Zhu, *Coord. Chem. Rev.*, 2019, **394**, 1–38.
17 S. Chen, W. Du, C. Qin, D. Liu, L. Tang, Y. Liu, S. Wang and M. Zhu, *Angew. Chem.*, 2020, **132**, 7612–7617.
18 Y.-H. Li, R.-W. Huang, P. Luo, M. Cao, H. Xu, S.-Q. Zang and T. C. W. Mak, *Sci. China: Chem.*, 2019, **62**, 331–335.
19 X.-H. Ma, J.-Y. Wang, J.-J. Guo, Z.-Y. Wang and S.-Q. Zang, *Chin. J. Chem.*, 2019, **37**, 1120–1124.
20 S.-H. Lu, Y. Li, S.-X. Yang, R.-D. Zhao, Z.-X. Lu, X.-L. Liu, Y. Qin, L.-Y. Zheng and Q.-E. Cao, *Inorg. Chem.*, 2019, **58**, 11793–11800.
21 A. K. Das, S. Biswas, S. S. Manna, B. Pathak and S. Mandal, *Inorg. Chem.*, 2021, **60**, 18234–18241.
22 R.-W. Huang, X.-Y. Dong, B.-J. Yan, X.-S. Du, D.-H. Wei, S.-Q. Zang and T. C. W. Mak, *Angew. Chem., Int. Ed.*, 2018, **57**, 8560–8566.
23 X.-S. Du, B.-J. Yan, J.-Y. Wang, X.-J. Xi, Z.-Y. Wang and S.-Q. Zang, *Chem. Commun.*, 2018, **54**, 5361–5364.
24 X.-Y. Dong, H.-L. Huang, J.-Y. Wang, H.-Y. Li and S.-Q. Zang, *Chem. Mater.*, 2018, **30**, 2160–2167.
25 M. Zhao, S. Huang, Q. Fu, W. Li, R. Guo, Q. Yao, F. Wang, P. Cui, C.-H. Tung and D. Sun, *Angew. Chem., Int. Ed.*, 2020, **59**, 20031–20036.
26 M. Cao, R. Pang, Q.-Y. Wang, Z. Han, Z.-Y. Wang, X.-Y. Dong, S.-F. Li, S.-Q. Zang and T. C. W. Mak, *J. Am. Chem. Soc.*, 2019, **141**, 14505–14509.
27 R.-W. Huang, Y.-S. Wei, X.-Y. Dong, X.-H. Wu, C.-X. Du, S.-Q. Zang and T. C. W. Mak, *Nat. Chem.*, 2017, **9**, 689–697.
28 S. Das, T. Sekine, H. Mabuchi, S. Hossain, S. Das, S. Aoki, S. Takahashi and Y. Negishi, *Chem. Commun.*, 2023, **59**, 4000–4003.
29 Z.-Y. Wang, M.-Q. Wang, Y.-L. Li, P. Luo, T.-T. Jia, R.-W. Huang, S.-Q. Zang and T. C. W. Mak, *J. Am. Chem. Soc.*, 2018, **140**, 1069–1076.
30 X.-Y. Dong, Y. Si, J.-S. Yang, C. Zhang, Z. Han, P. Luo, Z.-Y. Wang, S.-Q. Zang and T. C. W. Mak, *Nat. Commun.*, 2020, **11**, 1–9.
31 A. K. Das, S. Biswas, A. Thomas, S. Paul, A. S. Nair, B. Pathak, M. S. Singh and S. Mandal, *Mater. Chem. Front.*, 2021, **5**, 8380–8386.
32 W. A. Dar, A. Jana, K. S. Sugi, G. Paramasivam, M. Bodiuzzaman, E. Khatun, A. Som, A. Mahendranath, A. Chakraborty and T. Pradeep, *Chem. Mater.*, 2022, **34**, 4703–4711.

33 C. Xu, M.-M. Sheng, H.-T. Shi, M. Strømme and Q.-F. Zhang, *Dalton Trans.*, 2019, **48**, 5505–5510.
34 X.-H. Wu, P. Luo, Z. Wei, Y.-Y. Li, R.-W. Huang, X.-Y. Dong, K. Li, S.-Q. Zang and B. Z. Tang, *Adv. Sci.*, 2019, **6**, 1801304.
35 Z. Wang, Y.-M. Sun, Q.-P. Qu, Y.-X. Liang, X.-P. Wang, Q.-Y. Liu, M. Kurmoo, H.-F. Su, C.-H. Tung and D. Sun, *Nanoscale*, 2019, **11**, 10927–10931.
36 S. Biswas, A. K. Das, A. Nath, S. Paul, M. S. Singh and S. Mandal, *Nanoscale*, 2021, **13**, 17325–17330.
37 M. J. Alhilaly, R.-W. Huang, R. Naphade, B. Alamer, M. N. Hedhili, A.-H. Emwas, P. Maity, J. Yin, A. Shkurenko, O. F. Mohammed, M. Eddaoudi and O. M. Bakr, *J. Am. Chem. Soc.*, 2019, **141**, 9585–9592.
38 H. Schmidbaur and A. Schier, *Angew. Chem., Int. Ed.*, 2015, **54**, 746–784.
39 Z. Xiang, Y. Jiang, C. Cui, Y. Luo and Z. Peng, *Molecules*, 2022, **27**, 6749.
40 B.-L. Hou, D. Tian, J. Liu, L.-Z. Dong, S.-L. Li, D.-S. Li and Y.-Q. Lan, *Inorg. Chem.*, 2016, **55**, 10580–10586.